iScience

CellPress
OPEN ACCESS

Article

High-resolution assessment of coal mining methane emissions by satellite in Shanxi, China

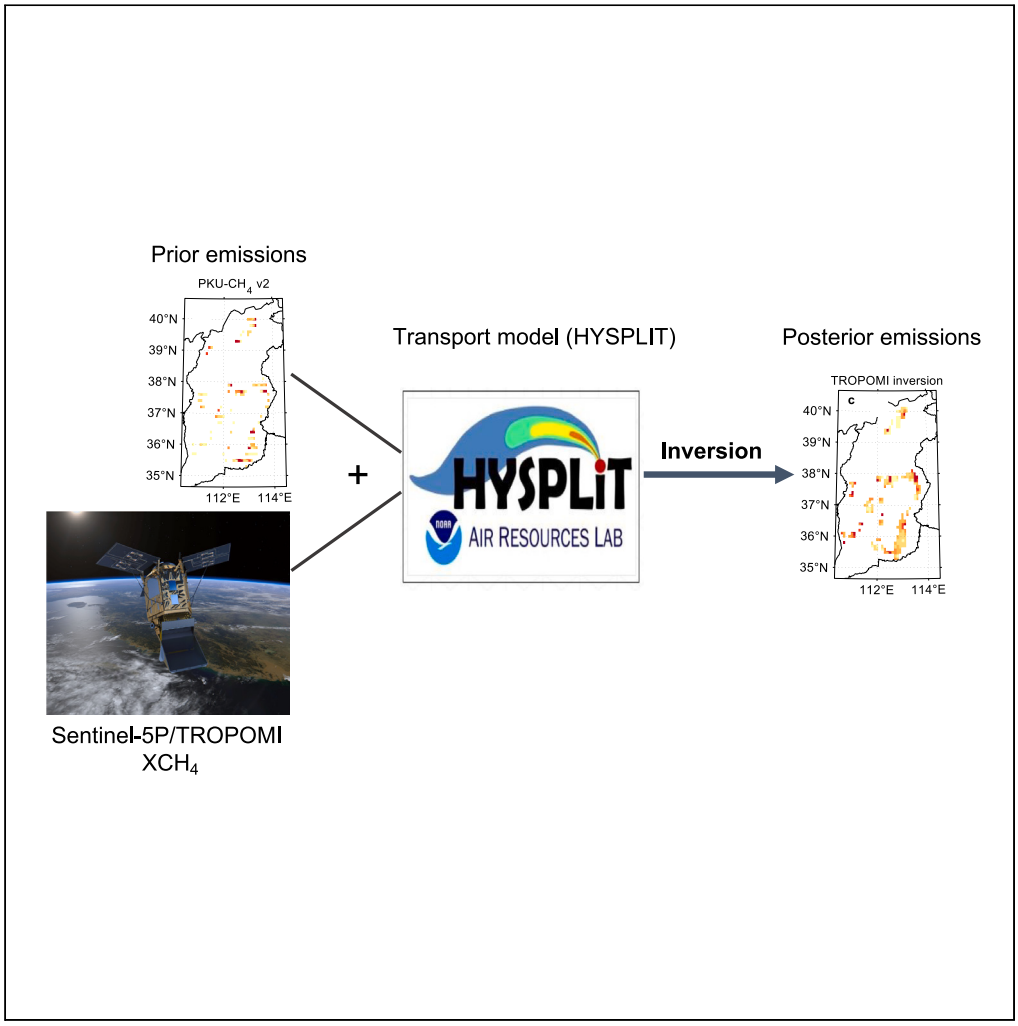

Shushi Peng, Clément Giron, Gang Liu, ..., Hugo de Almeida Rodrigues, Marielle Saunois, Philippe Ciais

speng@pku.edu.cn

Highlights

We assimilated TROPOMI images to inverse regional coal mining methane emissions

The inversed CH_4 emissions are close to upper bound of current bottom-up estimates

The CH_4 emission factors increase with coal mining depth at prefecture levels

We highlight potential of monitoring CH_4 leakages and emissions from satellites

Peng et al., iScience *26*, 108375
December 15, 2023
https://doi.org/10.1016/j.isci.2023.108375

iScience

CellPress
OPEN ACCESS

Article

High-resolution assessment of coal mining methane emissions by satellite in Shanxi, China

Shushi Peng,[1,6,7,*] Clément Giron,[2,6] Gang Liu,[1] Alexandre d'Aspremont,[2,3] Antoine Benoit,[2] Thomas Lauvaux,[4] Xin Lin,[4] Hugo de Almeida Rodrigues,[2] Marielle Saunois,[4] and Philippe Ciais[4,5]

SUMMARY

Accurate assessment of coal mine methane (CMM) emissions is a prerequisite for defining baselines and assessing the effectiveness of mitigation measures. Such an endeavor is jeopardized, however, by large uncertainties in current CMM estimates. Here, we assimilated atmospheric methane column concentrations observed by the TROPOMI space borne instrument in a high-resolution regional inversion to estimate CMM emissions in Shanxi, a province representing 15% of the global coal production. The emissions are estimated to be 8.5 $\pm$ 0.6 and 8.6 $\pm$ 0.6 Tg CH_4 yr^{-1} in 2019 and 2020, respectively, close to upper bound of current bottom-up estimates. Data from more than a thousand of individual mines indicate that our estimated emission factors increase significantly with coal mining depth at prefecture level, suggesting that ongoing deeper mining will increase CMM emission intensity. Our results show robustness of estimating CMM emissions utilizing TROPOMI images and highlight potential of monitoring methane leakages and emissions from satellites.

INTRODUCTION

China is the world's largest anthropogenic methane (CH_4) emitter since the 2000s.[1,2] Coal mining is the largest contributor, accounting for 40%–45% of China's anthropogenic CH_4 emissions and ~5% of global anthropogenic emissions.[3–5] During the 2000s, CH_4 emissions from coal mining in China increased by 12 Tg CH_4 yr^{-1} ([6–18] Tg CH_4 yr^{-1}, 95% confidence interval; ref.[4]), contributing 85% and 32% to the increase of China's and global anthropogenic CH_4 emissions, respectively.[2–4] To mitigate climate change, it is urgent for China to curb CH_4 emissions, especially in the coal industry. This requires a solid knowledge of current emissions, including the spatial details (e.g., distribution) about the most emitting areas or sites, in order to target the most effective measures and prioritize mitigation actions.[6]

Both bottom-up and top-down approaches give evidence for an increase in CH_4 emissions from coal mining in China during the 2000s.[3,4,7,8] Yet, they disagree in the magnitude of the trend,[2,8–10] ranging from 0.7 to 1.4 Tg CH_4 yr^{-2}. Furthermore, more recent bottom-up inventory data show a stabilization of coal methane emissions in the 2010s, mainly due to a stabilized coal production.[2,4] In contrast, recent top-down estimates suggested either a significant increase in those emissions after 2010 (0.9–1.1 Tg CH_4 yr^{-2}; ref.[11,12]) or a small increase (0.1–0.3 Tg CH_4 yr^{-2}; ref.[13,14]). Differences among inversions could be due to the use of different prior emissions, sparse atmospheric CH_4 concentrations measurements from surface stations, and previous satellites with coarse resolution (e.g., GOSAT), making it difficult to constrain emission hotspots from coal mines.[4] Overall, current top-down inversion estimates of the magnitude and trend in coal methane emissions in China are not consistent enough with each other to evaluate or improve bottom-up inventories.

The Sentinel-5P/TROPOMI (TROPOspheric Monitoring Instrument) mission, launched in 2017, collects daily images of the CH_4 column mole fractions (XCH_4) at high spatial resolution (5 km × 7 km) since 2018. The TROPOMI images have been used to detect and quantify large point sources in the oil and gas production sector, including ultra-emitters,[15–17] and regional extraction basins.[18] Coal mine emissions from Australia have been recently examined using TROPOMI.[19] Here, we focus on coal mining emissions from China, the largest coal producer of the world, and more specifically from the Shanxi Province. Shanxi represents about 15% of the global coal production, with more than 239 mines producing more than 0.5 million tons of coal annually (Figure 1). We assembled a detailed inventory data for 1,012 coal mines in the Shanxi, including mining depth, coal production and quality types, reported CH_4 ventilation/leak rates, recovery etc (see STAR Methods). The Shanxi province is suitable for TROPOMI's monitoring capabilities to assess coal methane emissions using high-resolution

[1]Sino-French Institute for Earth System Science, College of Urban and Environmental Sciences, and Laboratory for Earth Surface Processes, Peking University, Beijing, China
[2]Kayrros, 33 rue Lafayette, 75009 Paris, France
[3]CNRS & DI, Ecole Normale Supérieure, Paris, France
[4]Laboratoire des Sciences du Climat et de l'Environnement, LSCE/IPSL, CEA-CNRS-UVSQ, Université Paris-Saclay, 91191 Gif-sur-Yvette, France
[5]The Cyprus Institute, 20 Konstantinou Kavafi Street, 2121 Nicosia, Cyprus
[6]These authors contributed equally
[7]Lead contact
*Correspondence: speng@pku.edu.cn
https://doi.org/10.1016/j.isci.2023.108375

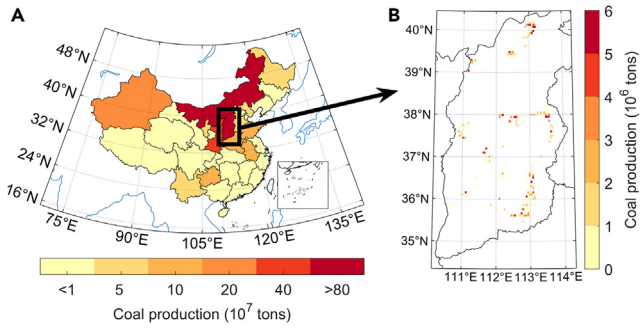

Figure 1. Distribution of coal production in China

Map of the coal production at province level in 2019 over China (A) and distribution of gridded coal mines with annual production larger than 0.6 million tons year^{-1} with a spatial resolution of 0.1 ° × 0.1 ° in the Shanxi Province.

(B) The coal production at each 0.1 ° × 0.1 ° grid cell represents the sum of production of all coal mines located at the grid cell. Note that the distribution of coal mines in the Shanxi Province in (B) is from the ground survey dataset conducted in 2011, but is scaled by the ratio of total coal production between 2011 and 2019 in the Shanxi Province.

regional inversions. We intend here to support the improvement of bottom-up inventories by not only assessing provincial total emissions, but also by identifying groups of mines with the highest emission rates.

We assimilated the TROPOMI methane column mixing ratio bias corrected level 2 products in a high-resolution regional inversion to estimate CH_4 emissions from coal production in the Shanxi province. The inversion assumes a prior map of emissions based on an annual (thus flat monthly) bottom-up inventory, with many mines but a uniform emission factor (see STAR Methods; PKU-CH_4 v2; ref.[4]). The XCH_4 plumes generated by grid cells (0.1 ° × 0.1 °) containing at least one coal mine are simulated by the Hybrid Single-Particle Lagrangian Integrated Trajectory model[20] (HYSPLIT). The nested version of HYSPLIT is similar to that used in previous regional inversion of TROPOMI observations[16] and the posterior map of emissions is obtained from the Bayesian inference of maximum a posteriori estimates for the prior emission estimates. In other words, the posterior emission rates are optimized by minimizing the distance between the modeled and TROPOMI-observed XCH_4 enhancements within images for each satellite overpass (see STAR Methods). We perform an ensemble of sensitivity tests with inversions to assess the uncertainty of posterior emissions, from TROPOMI XCH_4 measurement errors, background estimation method, meteorological data, and other key parameters of the inversion (see STAR Methods). To evaluate the impact of the prior emissions choice on posterior emissions, we also perform an inversion with no prior knowledge (see STAR Methods). Then we compare bottom-up inventories including EDGAR v6.0, Global Fuel Exploitation Inventory (GFEI v2) and PKU-CH_4 v2, with our independent top-down estimate derived from TROPOMI-based inversions. We further hypothesize that the CH_4 emission factor of coal mining (EF_{coal}) should be related to the depth of mining and the quality of coal that relates to different methane concentration in coal seams.[21–23] Taking advantage of the fact that our inversion has a very high resolution and can distinguish between different groups of mines, we finally examine the relationships between the EF_{coal} calculated from the inversion, and mining depth/coal types. This analysis provides direct insights to evaluate the bottom-up inventories emission factors.

RESULTS AND DISCUSSION

CH_4 emissions estimated by TROPOMI

Methane emissions from large coal mines or clusters of mines produce plumes of high XCH_4, which can be detected by TROPOMI (Figure 2A). Each large XCH_4 enhancement in the Shanxi Province is found to be associated with an ultra-emitter or a cluster of high-emitters, systematically assessed from 112 images of TROPOMI from 2019 to 2020, selecting only images with more than 30% of valid pixels (see STAR Methods). As expected, the averaged XCH_4 enhancement map during 2019–2020 reconstructed using the optimized posterior emissions shows better agreement with the observed one (Pearson correlation and significance by t test in this study; $r = 0.84$, $p < 0.001$) compared to the one based on the prior emissions ($r = 0.42$, $p < 0.001$) from the bottom-up inventory of PKU-CH_4 v2 (Figures 2A–2C). Figure 2D shows that the (spatial) correlation coefficients between observed XCH_4 enhancements from TROPOMI images and those reconstructed from posterior emissions are higher than those modeled from prior emissions, with a mean correlation coefficient of 0.71 for posterior emissions compared to 0.31 for prior emissions across the 112 images. Moreover, the posterior emissions capture 77% of the magnitude of observed XCH_4 enhancements from the 112 TROPOMI images on average, much higher than the 51% explained by the prior emissions. In order to test the sensitivity of our inversions to meteorological data, parameters and background concentration choices for our inversions, we performed an ensemble of inversions for these uncertainties (see STAR Methods). As a result, we found that the TROPOMI images can well constrain the methane emissions from coal mines in Shanxi with an uncertainty less than 10% (Figures 1 and 2).

Even with an agnostic flat monthly prior, our inversion estimates based on TROPOMI ($INV_{TROPOMI}$) produce a seasonal variation of monthly coal production in 2019 and 2020 ($r = 0.54$, $p = 0.015$; Figure 3A). Interestingly, $INV_{TROPOMI}$ detect also a drop and rise of emissions that corresponds with the Spring Festival of 2019, and a drop of 0.1 Tg CH_4 month^{-1} (14%) reflecting the impact of the COVID-19 outbreak on coal

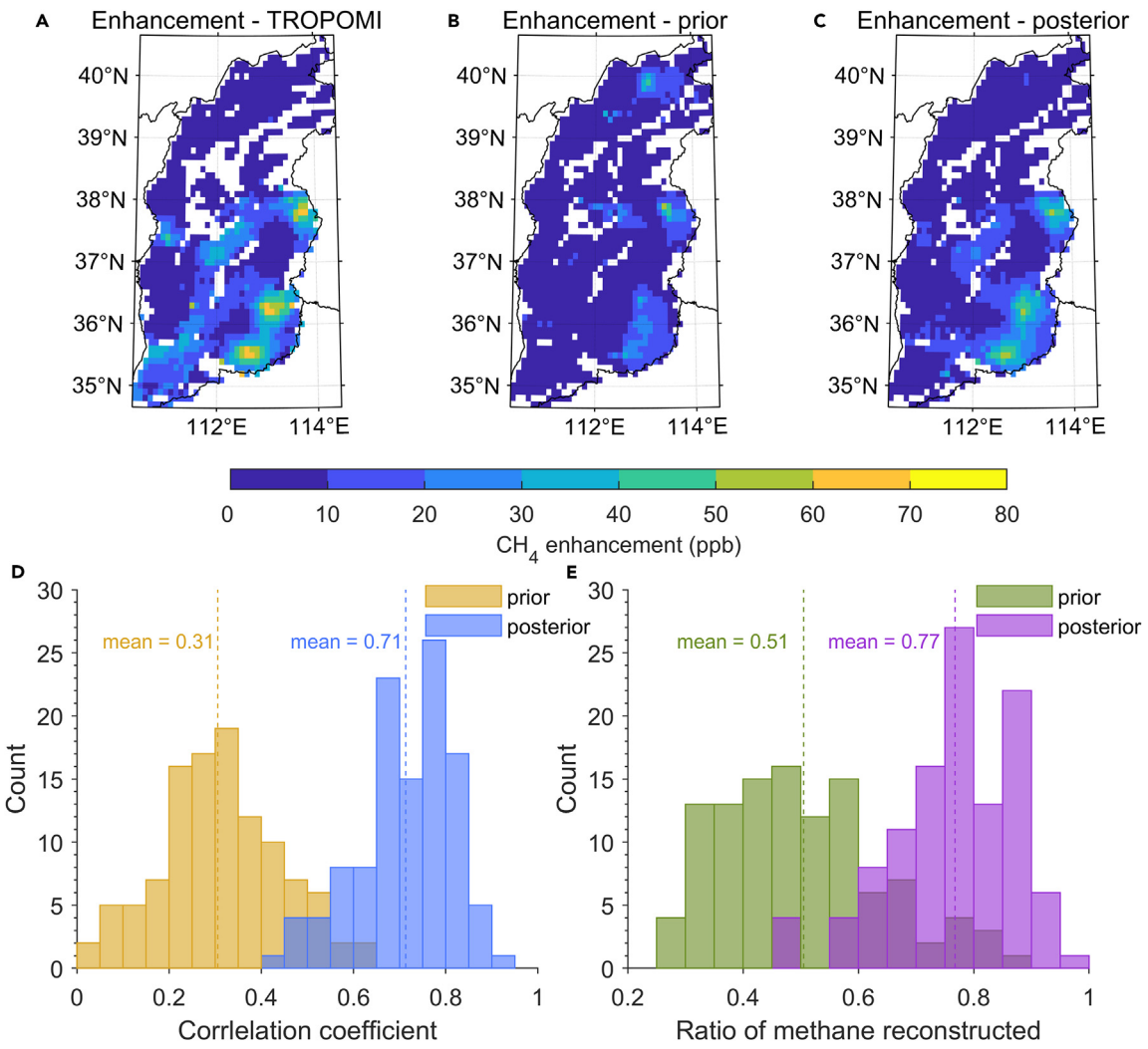

Figure 2. Spatial patterns of XCH_4 enhancement from TROPOMI, reconstructed XCH_4 using prior and posterior emissions, with a spatial resolution of 0.1 ° × 0.1 °

(A) averaged XCH_4 enhancement from 112 images of TROPOMI in 2019 and 2020; (B and C) reconstructed XCH_4 enhancement using prior and posterior emissions corresponding to the 112 images from TROPOMI.

(D) Frequency distribution of correlation coefficients between TROPOMI observations and prior (yellow) and posterior (blue) XCH_4 enhancement on an image-by-image basis.

(E) Frequency distribution of percentage of XCH_4 reconstructed by prior (green) and posterior (purple) estimates.

production, which decreased by more than 5% in February 2020. A subsequent recovery of production capacity in the next two months is also apparent in Figure 3A. Note that the reduction of $INV_{TROPOMI}$ (4% between the first three months of 2020 compared to December 2019) is smaller than that in coal production (~20%) during the COVID regulation period, which may result from uncertainties at monthly scales from both coal production of statistical bureau and $INV_{TROPOMI}$. Overall, the seasonal variation of monthly $INV_{TROPOMI}$ could be captured roughly, although there are relatively large uncertainties of $INV_{TROPOMI}$ in some months. Coal mining in Shanxi emitted 8.5 ± 0.6 (±1-sigma confidence interval) Tg CH_4 yr^{-1} in 2019 from $INV_{TROPOMI}$ results and 8.6 ± 0.6 Tg CH_4 yr^{-1} in 2020, respectively (Figure 3B). The total emissions from $INV_{TROPOMI}$ are higher than those from PKU-CH_4 v2 (5.8 ± 0.5 Tg CH_4 yr^{-1}) and GFEI v2 (7.3 ± 2.0 Tg CH_4 $year^{-1}$), but similar to EDGAR v6.0 (8.8 Tg CH_4 yr^{-1}).

Regarding the spatial distribution of emissions inferred by $INV_{TROPOMI}$ within Shanxi, hotspots are detected in most grids that contain high coal production mines (Figures 1 and 3). However, $INV_{TROPOMI}$ retrieves additional emission hotspots that were missing in our priori emission map (e.g., high-emissions grids in the southwest; Figure 3). In contrast to the agnostic inversion with no prior, the spatial distribution of emissions from coal mines in EDGAR v6.0, GFEI v2, and PKU-CH_4 v2 depends on activity data such as mine locations and production and emission factors. The three bottom-up inventories have different spatial patterns, but they all miss the high-emission hotpots found by

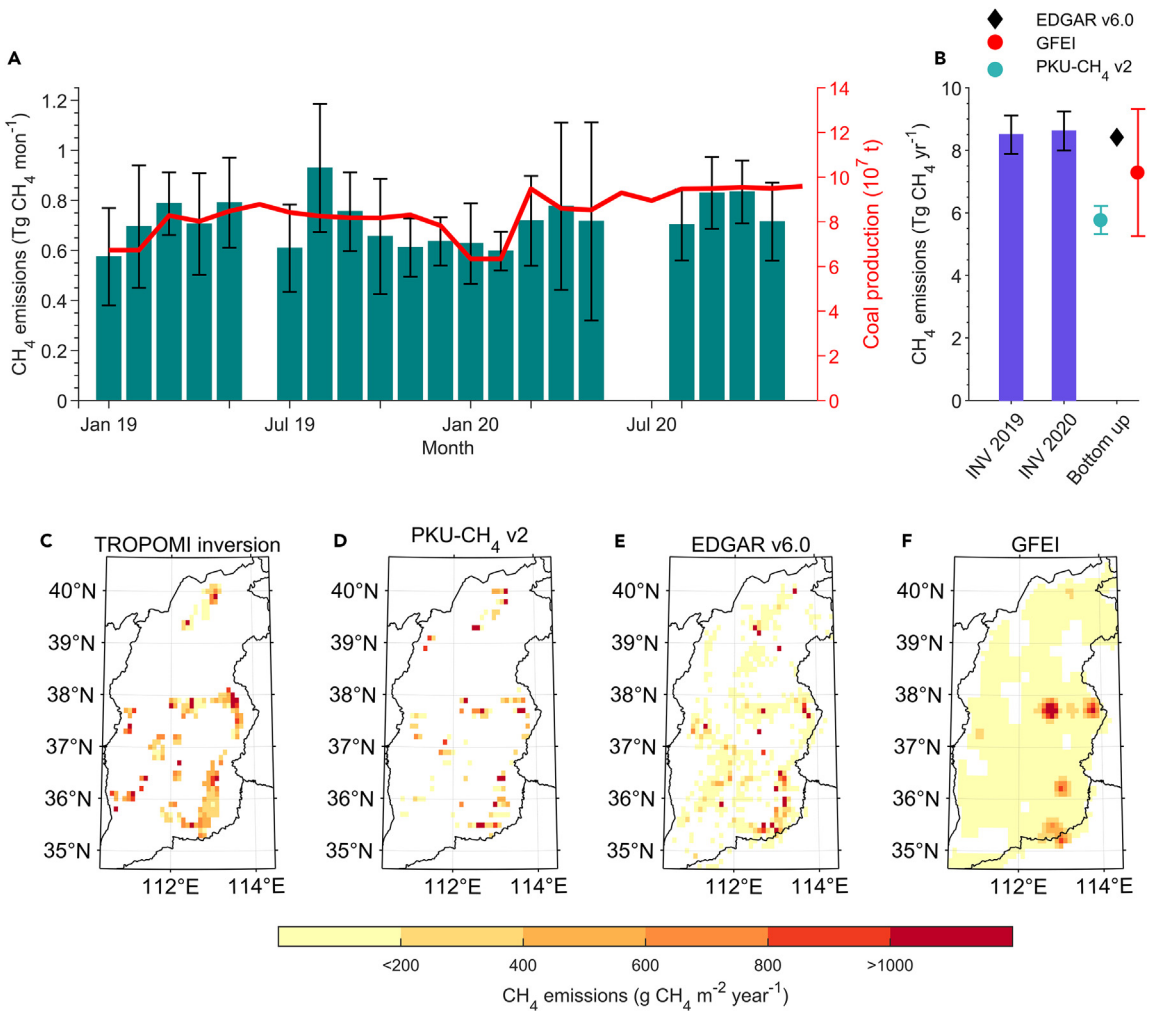

Figure 3. CH_4 emissions from coal mining in Shanxi

(A) Monthly CH_4 emissions from coal mining from January of 2019 to December of 2020 (green bars) and coal production (red line). The total annual coal mining emissions of Shanxi province estimated from inversion by TROPOMI ($INV_{TROPOMI}$) and three bottom-up inventories in 2019 (PKU-CH_4 v2, EDGAR v6.0 and GFEI) are summarized in (B). The error bars show standard deviation of the inversion ensemble from $INV_{TROPOMI}$. Note that the data of $INV_{TROPOMI}$ in Jun 2019, Jun 2020, Jul 2020, and Dec 2020 are missing because valid images are not enough for these months (<2) for the inversion. EDGAR v6.0 only provides the annual emission until 2018, so we scaled the coal mine emissions in 2019 by the ratio of coal production between 2019 and 2018.

(C–F) show the spatial pattern of CH_4 emissions from $INV_{TROPOMI}$ and bottom-up inventories (PKU-CH_4 v2, EDGAR v6.0 and GFEI) for Shanxi in 2019.

the inversion in the southwest, representing 10% of total emissions (Figures 3D–3F). We found that EDGAR v6.0, GFEI v2, and PKU-CH_4 v2 used an outdated coal production map from around 2011 to spatialize the total province-level emissions (from the product of an uniform emission factor and total coal production at province level) into each grid cell of their emission maps.[2,24,25] Some coal mines closed while new coal mines have opened since 2011,[26] which could explain the bias in the spatial distribution of CH_4 emissions from coal mines in the bottom-up inventories, compared to $INV_{TROPOMI}$. The $INV_{TROPOMI}$-optimized CH_4 emission map thus gives insights on local hotspots and how their emissions change at monthly or sub-monthly scale, although 4 out of 24 months are not covered by the inversion due to none or only one image available (see Figure S1), which should further be solved by future satellite missions.[16] This method can help improving not only the total emission of the basin, but also the spatial distribution map of coal emissions, and provides timely, updated estimates to evaluate bottom-up inventories.

CH_4 emission factor increases with mining depth

Combining $INV_{TROPOMI}$ estimate emissions at 0.1 ° × 0.1 ° with coal production data available at prefecture level in 2019 and 2020, we deduced an inversion-based average emission factor of coal methane emission (EF_{coal}) for each of the ten prefectures of Shanxi (see STAR Methods; Figure 4). This inversion-based EF_{coal} varies by more than one order of magnitude between prefectures, from 0.9 m^3 t^{-1}

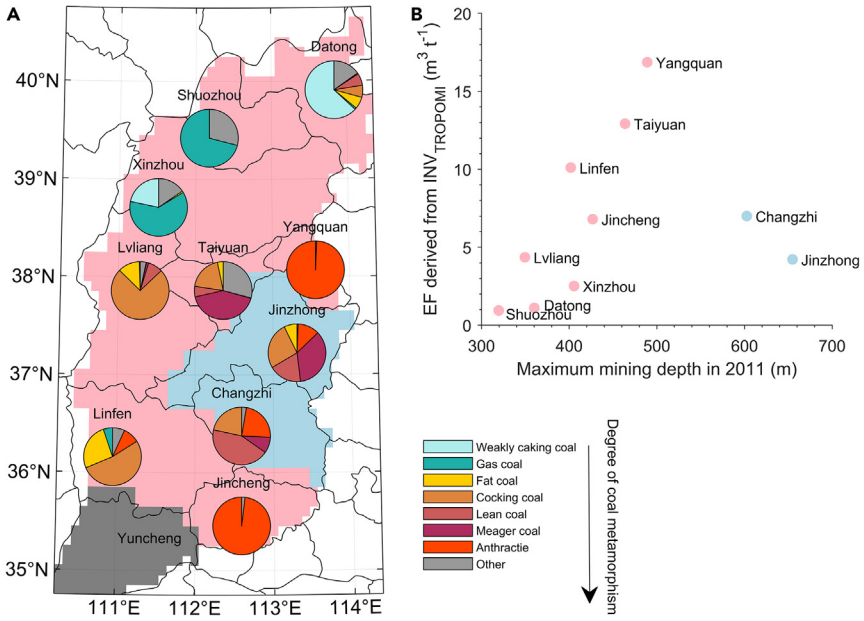

Figure 4. The relationship between emission factor (EF) of coal mining with depth of mining and the quality of coal

(A) The composition of the coal production by coal types for each prefecture in Shanxi.

(B) The relationship between average maximum mining depth and the emission factor (EF) of coal methane emissions derived from TROPOMI top-down inversion ($INV_{TROPOMI}$) in Shanxi at prefecture level. Note that the color of dots in (B) corresponds to the background color in (A), with the blue denoting Jinzhong and Changzhi, the two prefectures having deeper coal seams due to crustal subsidence in three tectogenesis after coal formation in the Carboniferous-Permian.[30,31]

in Shuozhou to 16.9 m^3 t^{-1} in Yangquan. Across the ten prefectures, this EF_{coal} shows marginally significant correlation with that from the ground inventory (r = 0.60, p = 0.067; see Figure S2). That inventory was conducted in 2011 and estimated potential fugitive emissions from underground mining without taking account of coal methane utilization that already has been adopted in Shanxi (the $INV_{TROPOMI}$ assesses actual coal methane emissions including their fractional reduction from methane utilization/recovery), which explains the smaller EF_{coal} in $INV_{TROPOMI}$ (see Figure S2). In addition, China's energy reforms in the past decade led to the reorganization and closure of some Shanxi coal mines with large emission and/or low methane utilization rates.[27] The large variation of EF_{coal} between prefectures highlights again that the use of the same EF_{coal} for all types of mines in a region, as done in bottom-up inventories (e.g., EDGAR v6.0, PKU-CH_4 v2), could lead to strong biases in the distribution of coal CH_4 emissions.

The large spatial variations in EF_{coal} found between prefectures are expected to be related to coal rank and mining depth.[21] For example, in the northern Shanxi where the coal seams in Datong, Shuozhou, and Xinzhou are shallow, and mostly weakly caking coal and gas coal with low metamorphic degree, we found low EF_{coal} values (Figure 4A). On the contrary, in Yangquan where the coal is mainly deep anthracite, we found the highest EF_{coal}. As the degree of metamorphism of anthracite increases, methane in the interstices of coal seams could decrease, which may explain the lower EF_{coal} in Shuozhou (mainly gas coal) than in Yangquan (mainly anthracite).

The gas pressure of coal seam increases with depth, and so does the volume of methane contained in coal. Thus, depth-specific EF_{coal} was suggested by the Intergovernmental Panel on Climate Change methodology,[28,29] with default EF_{coal} of 10 m^3 t^{-1}, 18 m^3 t^{-1}, and 25 m^3 t^{-1} for mines with depth less than 200 m, 200–400 m, and deeper than 400 m, respectively. Among different coal ranks (coalification), a higher rank coal generally has a higher methane content,[23] and thus accounts for a steeper increase in EF_{coal} with depth.[21,22] Almost 99% of the coal is produced from underground mines in Shanxi. Mining depth shows large spatial variations from less than 100 m to more than 700 m (see Figure S3), leading to large spatial variations in EF_{coal}. We thus regressed the EF_{coal} derived from $INV_{TROPOMI}$ against the average mining depth (from the year 2011) for each prefecture and found a high correlation (r = 0.88, p = 0.005) when excluding Changzhi and Jinzhong prefectures which are outliers (Figure 4B). The EF_{coal} in these two prefectures could be explained by substantial subsidence of coal seams in Jinzhong and Changzhi in the tectogenesis after the Carboniferous-Permian when coal was formed[30,31] (e.g., depth of 600 m coal seam in Jinzhong similar as ~400 m coal seam in Changzhi or Linfen). The relationship shown in Figure 4B suggests that EF_{coal} in these eight prefectures of Shanxi increases by 9.0 m^3 t^{-1} for a 100 m increase in the mining depth. A similar empirical function between coal mining depth and EF_{coal} was included in the inventory of 2011 across the eight prefectures[22] (r = 0.67, p = 0.07; see Figure S4). However, at the coal mine scale, this relationship could be weakened by the variability of coal ranks in different coal mines (see Figure S4). Note that the positive correlation between EF_{coal} and mining depth at prefecture level is derived with limited samples (n = 8), and this relationship also depends on the coal ranks and recovery or utilization of coal mine methane.[21–23] Thus, this relationship cannot be applicable in other regions unless regions have similar coal ranks and utilization of coal mine methane as Shanxi.

Uncertainties and limitations of the study

To analyze the uncertainty of our posterior emissions, we performed an ensemble of tests adding perturbations to the parameter values and input data (see STAR Methods). We found that the relative standard deviation of posterior emissions due to errors in XCH_4 retrievals (1.4%), the uncertain release duration as defined by the travel time between source locations and observed XCH_4 enhancements (15%), and the uncertainty of atmospheric transport (12%) are all relatively small compared to the standard deviation due to the uncertainty in background XCH_4 estimates (38%, see Figure S5). This suggests that the choice of background XCH_4 for calculating the XCH_4 enhancement is the most important parameter to accurately estimate CH_4 emissions. To test whether prior emission input affects the posterior emissions, we ran inversions without any prior knowledge (zero emission for each grid in Shanxi) and used a ridge regression to regularize the inverse problem (see STAR Methods). This sensitivity test gave similar total emissions as the Bayesian inversion with prior estimates from PKU-CH_4 v2, but with lower emissions in the north and higher emissions in the middle of Shanxi (see Figures S6 and S7). On average, there are two to six images per month (some months have 11–12 images) from TROPOMI fulfilling our quality filter with >30% of valid pixels (see Figure S1), but for some months no image was available (e.g., June in 2019, June and July in 2020). Future satellite missions (e.g., MethaneSAT[32]) complementary with TROPOMI would help better constrain the seasonal variations in emissions shown in Figure 3A. In addition, coal mines field campaigns for coal mine methane emissions during the days when high-resolution XCH_4 images from satellites are available can further be used to evaluate top-down inversions in the future.

Conclusions

Overall, we show that successive TROPOMI images of XCH_4 can constrain monthly CH_4 emissions from coal mining in Shanxi well, with annual emission estimates of 8.5 ± 0.6 Tg CH_4 yr^{-1} and 8.6 ± 0.6 Tg CH_4 yr^{-1} in 2019 and 2020, respectively. The top-down inversion with TROPOMI XCH_4 suggests that the use of a weighted average emission factor from the ground inventory dataset established in 2011 underestimates CH_4 emissions from coal mining.[4,25] We further find that deeper mining entails larger emission factors, as shown across the prefectures in Shanxi, suggesting that emission factors are likely to increase if mining deepens in the future. In addition, province-level emission factor used in bottom-up inventories may smooth the spatial variation of emissions due to the variation of mining depth and coal types across the mines. As the TROPOMI-based inversion used in our study can capture seasonal variation of coal mining activity (especially the drop in emissions corresponding to the coal production decrease in February, 2020 after the outbreak of COVID-19), a near real-time emission map can be updated on a regular basis. Such a tool could help monitoring and verification of emissions as well as supporting mitigation toward climate neutrality targets.

STAR★METHODS

Detailed methods are provided in the online version of this paper and include the following:

- KEY RESOURCES TABLE
- RESOURCE AVAILABILITY
  - Lead contact
  - Materials availability
  - Data and code availability
- METHOD DETAILS
  - Satellite-based XCH_4 retrievals from TROPOMI
  - Bottom-up inventories for coal CH_4 emissions
  - Ground inventory from 1012 coal mines in 2011
  - TROPOMI-based top-down inversion

SUPPLEMENTAL INFORMATION

Supplemental information can be found online at https://doi.org/10.1016/j.isci.2023.108375.

ACKNOWLEDGMENTS

The study was supported by the National Key Research and Development Program (2022YFE0209100) and the National Natural Science Foundation of China (grant number 42325102). The authors thank J. Bastin, C. Lelong, O. Dhobb, and A. Rostand from Kayrros SAS for fruitful discussion.

AUTHOR CONTRIBUTIONS

S.P. and P.C. designed the study. C.G. performed the TROPOMI inversion with help of A.A., A.B., T.L., and H.d.A.R. G.L. updated PKU-CH_4 v2 inventory. S.P., C.G., and G.L. performed the analysis and created all the figures. S.P. drafted the manuscript. All authors contributed to commenting and writing on the draft manuscript.

DECLARATION OF INTERESTS

S.P. serves as consulting editor of *iScience* journal.

Received: March 1, 2023
Revised: July 25, 2023
Accepted: October 27, 2023
Published: November 2, 2023

REFERENCES

1. National Development and Reform Commission of the People's Republic of China (2012). Second National Communication on Climate Change of the People's Republic of China. https://unfccc.int/sites/default/files/resource/The%20Second%20National%20Communication%20on%20Climate%20Change%20of%20P.%20R.%20China.pdf.
2. Crippa, M., Guizzardi, D., Schaaf, E., Monforti-Ferrario, F., Quadrelli, R., Risquez Martin, A., Rossi, S., Vignati, E., Muntean, M., Brandao De Melo, J., et al. (2021). GHG Emissions of All World Countries - 2021 Report, EUR 30831 EN (Publications Office of the European Union).
3. Peng, S., Piao, S., Bousquet, P., Ciais, P., Li, B., Lin, X., Tao, S., Wang, Z., Zhang, Y., and Zhou, F. (2016). Inventory of anthropogenic methane emissions in Mainland China from 1980 to 2010. Atmos. Chem. Phys. *16*, 14545–14562.
4. Liu, G., Peng, S., Lin, X., Ciais, P., Li, X., Xi, Y., Lu, Z., Chang, J., Saunois, M., Wu, Y., et al. (2021). Recent Slowdown of Anthropogenic Methane Emissions in China Driven by Stabilized Coal Production. Environ. Sci. Technol. Lett. *8*, 739–746.
5. Saunois, M., Stavert, A.R., Poulter, B., Bousquet, P., Canadell, J.G., Jackson, R.B., Raymond, P.A., Dlugokencky, E.J., Houweling, S., Patra, P.K., et al. (2020). The Global Methane Budget 2000–2017. Earth Syst. Sci. Data *12*, 1561–1623.
6. Lu, Y.Y., Zhang, H.D., Zhou, Z., Ge, Z.L., Chen, C.J., Hou, Y.D., and Ye, M.L. (2021). Current Status and Effective Suggestions for Efficient Exploitation of Coalbed Methane in China: A Review. Energy Fuels *35*, 9102–9123.
7. Bergamaschi, P., Houweling, S., Segers, A., Krol, M., Frankenberg, C., Scheepmaker, R.A., Dlugokencky, E., Wofsy, S.C., Kort, E.A., Sweeney, C., et al. (2013). Atmospheric CH4 in the first decade of the 21st century: Inverse modeling analysis using SCIAMACHY satellite retrievals and NOAA surface measurements. J. Geophys. Res. Atmos. *118*, 7350–7369.
8. Thompson, R.L., Stohl, A., Zhou, L.X., Dlugokencky, E., Fukuyama, Y., Tohjima, Y., Kim, S.-Y., Lee, H., Nisbet, E.G., Fisher, R.E., et al. (2015). Methane emissions in East Asia for 2000–2011 estimated using an atmospheric Bayesian inversion. JGR. Atmospheres *120*, 4352–4369.
9. US EPA (US Enviromental Protection Agency) (2012). Global Anthropogenic Non-CO2 Greenhouse Gas Emissions: 1990-2030. https://www.epa.gov/global-mitigation-non-co2-greenhouse-gases/global-non-co2-ghg-emissions-1990-2030.
10. Gao, J., Guan, C., and Zhang, B. (2020). China's CH4 emissions from coal mining: A review of current bottom-up inventories. Sci. Total Environ. *725*, 138295.
11. Miller, S.M., Michalak, A.M., Detmers, R.G., Hasekamp, O.P., Bruhwiler, L.M.P., and Schwietzke, S. (2019). China's coal mine methane regulations have not curbed growing emissions. Nat. Commun. *10*, 303.
12. Yin, Y., Chevallier, F., Ciais, P., Bousquet, P., Saunois, M., Zheng, B., Worden, J., Bloom, A.A., Parker, R.J., Jacob, D.J., et al. (2021). Accelerating methane growth rate from 2010 to 2017: leading contributions from the tropics and East Asia. Atmos. Chem. Phys. *21*, 12631–12647.
13. Zhang, Y., Jacob, D.J., Lu, X., Maasakkers, J.D., Scarpelli, T.R., Sheng, J.X., Shen, L., Qu, Z., Sulprizio, M.P., Chang, J., et al. (2021). Attribution of the accelerating increase in atmospheric methane during 2010–2018 by inverse analysis of GOSAT observations. Atmos. Chem. Phys. *21*, 3643–3666.
14. Lu, X., Jacob, D.J., Zhang, Y., Maasakkers, J.D., Sulprizio, M.P., Shen, L., Qu, Z., Scarpelli, T.R., Nesser, H., Yantosca, R.M., et al. (2021). Global methane budget and trend, 2010–2017: complementarity of inverse analyses using *in situ* (GLOBALVIEWplus CH4 ObsPack) and satellite (GOSAT) observations. Atmos. Chem. Phys. *21*, 4637–4657.
15. Varon, D.J., McKeever, J., Jervis, D., Maasakkers, J.D., Pandey, S., Houweling, S., Aben, I., Scarpelli, T., and Jacob, D.J. (2019). Satellite Discovery of Anomalously Large Methane Point Sources From Oil/Gas Production. Geophys. Res. Lett. *46*, 13507–13516.
16. Lauvaux, T., Giron, C., Mazzolini, M., d'Aspremont, A., Duren, R., Cusworth, D., Shindell, D., and Ciais, P. (2022). Global assessment of oil and gas methane ultra-emitters. Science *375*, 557–561.
17. Irakulis-Loitxate, I., Guanter, L., Liu, Y.-N., Varon, D.J., Maasakkers, J.D., Zhang, Y., Chulakadabba, A., Wofsy, S.C., Thorpe, A.K., Duren, R.M., et al. (2021). Satellite-based survey of extreme methane emissions in the Permian basin. Sci. Adv. *7*, eabf4507.
18. Deng, Z., Ciais, P., Tzompa-Sosa, Z.A., Saunois, M., Qiu, C., Tan, C., Sun, T., Ke, P., Cui, Y., Tanaka, K., et al. (2022). Comparing national greenhouse gas budgets reported in UNFCCC inventories against atmospheric inversions. Earth Syst. Sci. Data *14*, 1639–1675.
19. Sadavarte, P., Pandey, S., Maasakkers, J.D., Lorente, A., Borsdorff, T., Denier van der Gon, H., Houweling, S., and Aben, I. (2021). Methane Emissions from Superemitting Coal Mines in Australia Quantified Using TROPOMI Satellite Observations. Environ. Sci. Technol. *55*, 16573–16580.
20. Stein, A.F., Draxler, R.R., Rolph, G.D., Stunder, B.J.B., Cohen, M.D., and Ngan, F. (2015). NOAA's HYSPLIT Atmospheric Transport and Dispersion Modeling System. Bull. Am. Meteorol. Soc. *96*, 2059–2077.
21. Kholod, N., Evans, M., Pilcher, R.C., Roshchanka, V., Ruiz, F., Coté, M., and Collings, R. (2020). Global methane emissions from coal mining to continue growing even with declining coal production. J. Clean. Prod. *256*, 120489.
22. Wang, Z., Wang, X., Zuo, W., Ma, X., and Li, N. (2019). The influence of temperature on methane adsorption in coal: A review and statistical analysis. Adsorp. Sci. & Technol. *37*, 745–763.
23. Zhou, Z., Shi, F., Zhang, Y., Yu, Y., and Tang, S. (2021). Influencing Factors of Gas Emission in Coal Mining Face. In held in Singapore, 2021, Q. Liang, W. Wang, X. Liu, Z. Na, X. Li, and B. Zhang, eds. (Springer Singapore), pp. 278–284.
24. Scarpelli, T.R., Jacob, D.J., Grossman, S., Lu, X., Qu, Z., Sulprizio, M.P., Zhang, Y., Reuland, F., Gordon, D., and Worden, J.R. (2022). Updated Global Fuel Exploitation Inventory (GFEI) for methane emissions from the oil, gas, and coal sectors: evaluation with inversions of atmospheric methane observations. Atmos. Chem. Phys. *22*, 3235–3249.
25. Sheng, J., Song, S., Zhang, Y., Prinn, R.G., and Janssens-Maenhout, G. (2019). Bottom-Up Estimates of Coal Mine Methane Emissions in China: A Gridded Inventory, Emission Factors, and Trends. Environ. Sci. Technol. Lett. *6*, 473–478.
26. National Energy Administration of the People's Republic of China (NEA) (2013). Shanxi plans to add 100 million tons of coal production capacity. http://www.nea.gov.cn/2013-05/03/c_132357516.htm.
27. Lu, P., Zhou, L., Cheng, S., Zhu, X., Yuan, T., Chen, D., and Feng, Q. (2020). Main challenges of closed/abandoned coal mine resource utilization in China. Energy Sources, Part A Recovery, Util. Environ. Eff. *42*, 2822–2830.
28. IPCC (2013). Climate Change 2013: The Physical Science Basis. Contribution of Working Group I to the Fifth Assessment Report of IPCC on Climate Change (Cambridge University Press).
29. IPCC (2019). IPCC in 2019 Refinement to the 2006 IPCC Guidelines for National Greenhouse Gas Inventories. https://www.ipcc.ch/report/2019-refinement-to-the-2006-ipcc-guidelines-for-national-greenhouse-gas-inventories/.
30. Sun, L., Jin, X., Wen, C., and Bian, P. (2009). The Structure and Seismic Activity Characteristics of Jinhuo Fault Zone, *27* (North China Earthquake Sciences), pp. 11–15.
31. Liu, K., Cao, D., Lin, Z., and Li, J. (2013). Subsidence history of central-northern Qinshui basin. Coal Geol. Explor. *41*, 8–11.
32. Jacob, D.J., Varon, D.J., Cusworth, D.H., Dennison, P.E., Frankenberg, C., Gautam, R., Guanter, L., Kelley, J., McKeever, J., Ott, L.E., et al. (2022). Quantifying methane emissions from the global scale down to point sources using satellite observations of atmospheric methane. Atmos. Chem. Phys. *22*, 9617–9646.
33. ESA (2022). S5P Mission Performance Centre Methane [L2__CH4___] Readme. V02.03.01. https://sentinel.esa.int/documents/247904/3541451/Sentinel-5P-Methane-Product-Readme-File.

34. GDAL/OGR Contributors (2022). Geospatial Data Abstraction Software Library. https://gdal.org.
35. Hasekamp, O.P., Lorente, A., Hu, H., Butz, A., Joost, Brugh, A.d., and Landgraf, J. (2019). Algorithm Theoretical Baseline Document for Sentinel-5 Precursor Methane Retrieval (SRON-S5P-LEV2-RP-001).
36. EIA (2022). Energy Information Administration (EIA). https://www.eia.gov/international/data/world.
37. Bureau of Statistics of Shanxi Province (2020). Shanxi Statistical Yearbook 2020 (China Statistics Press).
38. State Administration of Coal Mine Safety (SACMS) (2012). Compilation of National Coal Mine Gas Level Identification for 2011 (National Mine Safety Administration Press).
39. Liu, Z., Guan, D., Wei, W., Davis, S.J., Ciais, P., Bai, J., Peng, S., Zhang, Q., Hubacek, K., Marland, G., et al. (2015). Reduced carbon emission estimates from fossil fuel combustion and cement production in China. Nature *524*, 335–338.
40. Zhang, Y., Gautam, R., Pandey, S., Omara, M., Maasakkers, J.D., Sadavarte, P., Lyon, D., Nesser, H., Sulprizio, M.P., Varon, D.J., et al. (2020). Quantifying methane emissions from the largest oil-producing basin in the United States from space. Sci. Adv. *6*, eaaz5120.
41. Shen, L., Zavala-Araiza, D., Gautam, R., Omara, M., Scarpelli, T., Sheng, J., Sulprizio, M.P., Zhuang, J., Zhang, Y., Qu, Z., et al. (2021). Unravelling a large methane emission discrepancy in Mexico using satellite observations. Remote Sens. Environ. *260*, 112461.
42. Heald, C.L., Jacob, D.J., Jones, D.B.A., Palmer, P.I., Logan, J.A., Streets, D.G., Sachse, G.W., Gille, J.C., Hoffman, R.N., and Nehrkorn, T. (2004). Comparative inverse analysis of satellite (MOPITT) and aircraft (TRACE-P) observations to estimate Asian sources of carbon monoxide. J. Geophys. Res. *109*, D23306.
43. Pandey, S., Gautam, R., Houweling, S., van der Gon, H.D., Sadavarte, P., Borsdorff, T., Hasekamp, O., Landgraf, J., Tol, P., van Kempen, T., et al. (2019). Satellite observations reveal extreme methane leakage from a natural gas well blowout. Proc. Natl. Acad. Sci. USA *116*, 26376–26381.
44. Horvitz, D.G., and Thompson, D.J. (1952). A Generalization of Sampling Without Replacement from a Finite Universe. J. Am. Stat. Assoc. *47*, 663–685.
45. Elvidge, C., Zhizhin, M., Hsu, F.-C., and Baugh, K. (2013). VIIRS Nightfire: Satellite Pyrometry at Night. Remote Sens *5*, 4423–4449.

STAR★METHODS

KEY RESOURCES TABLE

REAGENT or RESOURCE	SOURCE	IDENTIFIER
Deposited data		
High resolution bottom-up inventory of methane emissions in China	This paper	https://figshare.com/s/b38a368111749f1412be
TROPOMI data	Copernicus Open Access Hub	https://scihub.copernicus.eu/
The meteorological reanalysis data used for the forward HYSPLIT simulations	Global Forecast System (GFS), Environmental Modeling Center, National Centers for Environmental Prediction (National Weather Service, NOAA, U.S. Department of Commerce, NCEI DSI 6182, gov.noaa.ncdc:C00634); and from the Global Data Assimilation System (GDAS), Environmental Modeling Center, National Centers for Environmental Prediction (National Weather Service, NOAA, U.S. Department of Commerce, NCEI DSI 6172, gov.noaa.ncdc:C00379).	https://www.ncei.noaa.gov/products/weather-climate-models/global-forecast https://www.emc.ncep.noaa.gov/emc_new.php https://www.ncei.noaa.gov/products/weather-climate-models/global-data-assimilation
CH_4 emissions from coal mine	EDGAR v6.0	https://edgar.jrc.ec.europa.eu
CH_4 emissions from coal mine	GFEI v2	https://doi.org/10.7910/DVN/HH4EUM.
Software and algorithms		
The HYSPLIT model	Air Resources Laboratory, NOAA	www.arl.noaa.gov/hysplit/
MATLAB R2022a	Commercially Available Software (Mathworks)	N/A

RESOURCE AVAILABILITY

Lead contact

Further information and requests can directed to Dr. Shushi Peng (speng@pku.edu.cn).

Materials availability

This study did not generate new physical materials.

Data and code availability

- All data used in this study is publicly available: TROPOMI data (S5P L2 CH4 OFFLINE) are available from the Copernicus Open Access Hub (https://scihub.copernicus.eu/). The meteorological reanalysis data used for the forward HYSPLIT simulations are available from the Global Forecast System (GFS), Environmental Modeling Center, National Centers for Environmental Prediction (National Weather Service, NOAA, U.S. Department of Commerce, NCEI DSI 6182, gov.noaa.ncdc:C00634); and from the Global Data Assimilation System (GDAS), Environmental Modeling Center, National Centers for Environmental Prediction (National Weather Service, NOAA, U.S. Department of Commerce, NCEI DSI 6172, gov.noaa.ncdc:C00379). PKU-CH_4 v2 is available at https://figshare.com/s/b38a368111749f1412be. EDGAR v6.0 is available at https://edgar.jrc.ec.europa.eu/. GFEI v2 is available at https://doi.org/10.7910/DVN/HH4EUM.
- The inversion method presented in this article is constructed using the HYSPLIT model (v4.2.0; 2019), which was developed by the Air Resources Laboratory at NOAA and is available from www.arl.noaa.gov/hysplit/. The code of inversion could be available on request from Dr. Clément Giron (Email: c.giron@kayrros.com).
- Any additional information required to reanalyze the data reported in this article is available from the lead contact on request.

METHOD DETAILS

Satellite-based XCH_4 retrievals from TROPOMI

We collected bias-corrected methane column mixing ratios derived from the spaceborne instrument TROPOMI on board of the Sentinel 5P satellite (ESA products of S5P L2 CH4 OFFLINE[33]). TROPOMI is an imaging spectrometer, orbiting the earth in near-polar, sun-synchronous trajectories with a mean local solar time ascending node at 13:30. TROPOMI's swath is approximately 2600 km wide, achieving near-global coverage on a daily basis. Our study relies on TROPOMI measurements from January 2019 to December 2020, with images collected over the

Shanxi Province shape, and re-projected on a 0.1°×0.1° regular grid using the GDAL library.[34] As cloud cover, high solar zenith angle, high viewing zenith angle, large terrain roughness or small surface albedo etc. induce substantial bias in XCH_4 retrievals,[33] we only used pixels with a quality assurance value (qa_value = 1). TROPOMI images were filtered to keep only those with more than 30% of valid pixels (qa_value =1). With this filter, 58 and 54 images were selected per year in 2019 and 2020 respectively. Uneven albedo and aerosol optical thickness are amongst the parameters influencing the quality and accuracy of TROPOMI XCH_4 retrievals. Although the data product we used in this study includes a correction based on surface albedo in the SWIR domain,[35] we also assessed the reliability of TROPOMI XCH_4 retrievals by evaluating its correlation with surface shortwave infrared albedo (Albedo) and aerosols optical thickness (AOD; see Figure S8). When using only high-quality pixels (qa_value = 1), R^2 scores of linear regressions between bias-corrected XCH_4 and Albedo (R^2=0.010) and AOD (R^2=0.006) are quite low, hence significant bias of XCH_4 from albedo or aerosols can be dismissed. When including medium-quality pixels (qa_value $\geq$ 0.4), the R^2 scores are estimated respectively at 0.007 and 0.130 for albedo and AOD, confirming that the albedo and aerosols has limited impact on XCH_4 retrievals in our region of interest.

Bottom-up inventories for coal CH_4 emissions

Three bottom-up inventories for annual methane emissions from coal mining in the Shanxi province were used in this study: PKU-CH_4 v2, EDGAR v6.0 and GFEI v2. PKU-CH_4 v2 was updated up to 2020 using annual coal production in 2020 from the latest Statistic Yearbook, following the bottom-up methodology in ref.[4]. The annual maps from PKU-CH_4 v2 were used as prior for our top-down inversion. For the EDGAR v6.0, we used the monthly gridded emissions of China in 2018, and then calculated the total emission as the sum of all grids in Shanxi province. We then scaled the emissions in 2018 from EDGAR v6.0 into emissions in 2019 by using the ratio of coal production of Shanxi in 2019 and 2018. This estimate is referred as EDGAR v6.0. The inventory of GFEI v2 gives the annual emissions that incorporate national reports of China to the United Nations Framework Convention on Climate Change (UNFCCC) and allocates the total national emissions into infrastructure locations from ref.[25] with a 0.1°×0.1° spatial resolution.[24] We used annual emissions of 2019 from GFEI v2 here, updated with IPCC emission factors and yearly activity data from US Energy Information Administration.[24,36] To validate seasonal variation of top-down monthly emissions, the monthly coal production of Shanxi province and yearly coal production in prefecture level were collected from Shanxi Statistic Yearbook.[37]

Ground inventory from 1012 coal mines in 2011

We collected the information of coal mines in Shanxi province publicly available in the ground inventory of the National Coal Mine Methane Level Identification for 2011, by the State Administration of Coal Mine Safety.[38] The coal production in Shanxi province increased by ~60% from 2011 to 2020. Emission factors from this inventory have been applied to estimate CH_4 emissions from coal mining in refs.[24,25]. We collected data from 1012 coal mines, more than 95% coal mines in Shanxi province, including annual coal production (537 coal mines), mining depth (984 coal mines) and emission factors (727 coal mines) reported in the ground inventory of 2011. The location of these coal mines were derived from Baidu Map Platform (http://api.map.baidu.com/lbsapi/getpoint/index.html). Note that 84 out of the 1012 coal mines are excluded in our analysis, as these 84 coal mines have been closed since 2016 because of a supply-side structural reform of the coal industry by eliminating low efficiency coal production.[27]

According to the ground inventory and the locations of coal mines, we aggregate the production and average the mining depth, extraction rate and emission factors weighted by the coal production into 0.1°×0.1° grid scale in 2011. For the map of coal production in 2019 (2020), we scaled the map of 2011 by the ratio of total province-level production in 2019 (2020) and in 2011. The main types of coal for each prefecture in Shanxi were collected from the dataset in ref.[39]. To compare the EF_{coal} derived from $INV_{TROPOMI}$ in 2019, we adjusted the EF_{coal} derived from ground inventory in 2011 by the composition of coal production mined from low gas mines, high gas mines and outburst gas mines in each prefecture between 2019 and 2011 in Figure S2.

TROPOMI-based top-down inversion

Model

The estimates are produced using a classical Bayesian regression framework.[40,41] Specifically, we solve the following quadratic programming problem for each useable TROPOMI XCH4 image

$$\begin{array}{ll} min_x & J(x) = (y - Kx)^T S_O^{-1}(y - Kx) + \lambda(x - x_P)^T S_p^{-1}(x - x_P) \\ s.t. & x \geq 0 \end{array}$$

where y is the methane column mixing ratio enhancement (i.e. methane column mixing ratio bias corrected image subtracted from its median value and with negative values clipped to 0); K is the methane dispersion footprints produced using the Hybrid Single-Particle Lagrangian Integrated Trajectory model[20] (HYSPLIT); x_P is the prior emission rates vector (all 0.1°×0.1° regular grid cells); S_O is the covariance matrix for observational error; S_p is the covariance matrix for prior error.[40,42]

If we omit the non-negativity constraint $x \geq 0$, this quadratic program can be solved in closed form by

$$x = x_P + \lambda^{-1} S_P K^T \left(\lambda^{-1} K S_P K^T + S_O\right)^{-1} (y - Kx_P)$$

and a condition number of this problem can be computed to assess the stability and robustness of the solution. This condition number is defined as $\kappa(\lambda) = \frac{\sigma_{max}(\tilde{S}_\lambda)}{\sigma_{min}(\tilde{S}_\lambda)}$ with σ_{max} (resp. σ_{min}) denoting the highest (resp. smallest) singular value of $\tilde{S}_\lambda = (K^T {S_O}^{-1} K + \lambda {S_P}^{-1})^{-1}$. We add the non-negativity constraint for x and solve the quadratic program numerically. This constraint regularizes the solution and limits overfit. λ is used to scale the relative weights of the TROPOMI XCH4 image and prior terms. It should ideally be equal to 0 or very small. Yet for several dates, the quadratic program is ill-conditioned due to the sparsity of the TROPOMI XCH4 image and near-colinearity of some HYSPLIT footprints ($\kappa(\lambda) \gg 0$). We ensure that the estimates for each date are produced by a well-conditioned minimization program by incrementing $\lambda \in [10^{-2}, 10^2]$ on a log_{10} scale up to the smallest value such that $\kappa(\lambda) < \tau$. We set $\tau = 10^3$ based on the criterions as explained in detail below.

The quadratic program solved at each date to estimate emission rates from grid cells is composed of one term controlling the fit of estimated emissions with TROPOMI observations, and one term forcing the solution to be close to some prior knowledge on the basin emitters. The second term is regularizing the inversion, and its weight should be kept as small as possible when TROPOMI retrievals are complete and reliable enough, and the HYSPLIT simulations matrix has a high rank. Hence, we use the minimum λ parameter that keeps the quadratic program well-conditioned. By construction, the condition number of the inversion should converge to that of S_p when λ increases (see Figure S9). We scale the system so that the condition number of S_p is 10. In our results, we pick the maximum acceptable condition number $\tau = 10^3$ which controls inversion error while ensuring that the corresponding regularizing coefficients λ have the following properties:

- *Percentage of methane reconstructed.* The proportion of methane reconstructed is steady (roughly 0.8) for small fixed values for λ, and decreases when $\lambda \ngeq 1$ (see Figure S10 middle panel). We pick the threshold so that the λ values correspond to the *"elbow"* of the bar chart in Figure S10 (middle), between 0.1 and 1, to regularize the system while avoiding over-penalization. Similarly, our condition number criterion yields more than 97% of λ values in $\{10^{-2}, 10^{-1}, 1\}$, and the corresponding proportion of methane reconstructed is 0.76 (Figure S10 middle panel).
- *Distribution of λ values.* λ values determined by the condition number criterion should mostly be smaller or equal to 1, as we want TROPOMI data to have more weight in the final output than the prior database. This distribution is shown on the top panel of Figure S10.
- *Degrees of freedom for signal (DOFS).* By construction, high λ values heavily reduce the degrees of freedom of the system by constraining the solution to be very close to the prior. Our condition number criterion preserves significant DOFS as in ref.[40], mostly in range [20-125] (see Figure S10 bottom panel).

Observational and prior error covariance matrices

S_O is computed using the relative residual error method.[42] In particular, we split our work domain into a 2°×2° grid and compute the standard deviation matrix of the residual error in the bias corrected subtraction of observed methane concentrations by simulated concentrations (derived from HYSPLIT simulations and prior PKU-CH_4 v2 emission rates). S_O is defined as the normalized, relative standard deviation matrix and, by construction, it accounts for both the sensor error and the model error. S_P is defined as the absolute error between the gridded inventories PKU-CH_4 v2 and EDGAR v6.0, re-projected on the same 0.1°×0.1° regular grid as the images. Both S_O and S_P are normalized so that their relative weight in the objective function J is fully controlled by the parameter λ. In addition, very small diagonal values of S_P are set at 1/10 of its maximal value (i.e. 0.1 after minmax normalization) to avoid ill-conditioning that would occur when EDGAR v6.0 and PKU-CH4 v2 have very similar values. In more than 97% of the daily inversions, the condition number criterion yields $\lambda \in \{10^{-2}, 10^{-1}, 1\}$, hence giving to the observational term a greater of equal weight with respect to the prior penalization term.

HYSPLIT simulations

Each grid pixel with a positive methane emissions value in the PKU-CH4 v2 inventory is considered as a potential source from which we simulate methane plumes using the Lagrangian particle dispersion model HYSPLIT. These simulations are executed in concentration, forward mode on a 0.01°×0.01° grid and re-projected on the priors and images 0.1°×0.1° grid. HYSPLIT parameters are mostly similar to those used in ref.[16]. Particles are released continuously at constant rate (10000 particles per hour) from a grid cell; each particle represents a fixed amount of methane spreading horizontally as a gaussian puff with respect to the meteorological fields. The Planetary Boundary Layer in which the particles diffuse vertically is derived from the meteorological data. The release altitude is set at 10 meters, consistent with the fact that methane is mainly emitted from coal mines through Ventilation Air Methane (VAM) devices located close to the ground level. Following the analysis of ref.[16] on the negligible impact of the parameters defining the mixed layer height model and vertical mixing strength, we keep these parameters at default value. These fields come from the Global Data Assimilation System (GDAS) meteorological data produced by the National Centers for Environmental Prediction (NCEP) at 1-degree spatial resolution and sampled hourly; they are downloaded from the NOAA FTP server. For sensitivity analysis purposes, we also rely on data from the Global Forecast System (GFS), also produced by NCEP at 0.25°×0.25° spatial and hourly temporal resolutions available on the same NOAA FTP server.

Release is set to start 10 hours before TROPOMI overpass time, assuming that the simulated plumes have reached a steady state at sensing time. This hypothesis is discussed and supported in next section. HYSPLIT plumes thereby obtained are normalised to produce footprints which play the same role as the Jacobian matrix derived from GEOS-FP data in refs.[40,41]

Uncertainty and sensitivity analysis

Sources of uncertainty for the Shanxi methane emissions estimates include the TROPOMI sensor error, uncertainty in the background estimation method, in the meteorological data used as input for HYSPLIT simulations, and in the HYSPLIT parameters. To account for the

modelling uncertainty, we perform an ensemble of inversion with perturbations of the parameters and input data. Notably, we evaluate the standard deviation of the methane emission estimates with respect to variations in meteorological data, simulation duration and methane background estimation process, respectively denoted σ_w, σ_d, σ_b. The sensitivity of meteorological data σ_w is performing the inversion using two different meteorological data sources, namely GFS 0.25 degree, GDAS 1 degree. The uncertainty induced by the choice of the parameters in the transport model, σ_d, mainly stems for the release duration parameter t_d used for simulating methane plumes (which are further normalized to produce the K matrix). We perform simulations for $t_d \in \{6, 8, 10, 12, 14\}$. The methane background concentration contributes significantly to the uncertainty on the methane emissions. We compute the standard deviation of the emission estimates when the background is either the first, second, third quartile of each image. We also use a setting where the background value is the TROPOMI image median and where all pixels below median + std are set to 0 (i.e. small enhancements are considered as noisy values and are not taken into account). The standard deviation of this ensemble is denoted σ_b. We also propagate the TROPOMI error, as provided by the *precision* data product,[43] to derive the sensor measurement error σ_m. Figure S5 shows the marginal sensitivity distributions (σ_m, σ_b, σ_d and σ_w on an image-per-image basis) and highlights the strong impact of the background computation method on the emission estimates (mean relative standard deviation is 38%), which influences the output much more than the meteorological data choice and the release duration. The TROPOMI measurement error has a negligible effect on the emission estimates.

We also account for the absence of valid readings for some days (namely sampling uncertainty σ_s) by using a poll setting and deriving σ_s from the unbiased Horvitz-Thompson confidence bounds.[44] For a given period of time, each processed image produces a methane emission flux rate that is observed and each date without image produces a non-observed flux rate. Considering a poll plan with equal probabilities, we derive the sampling uncertainty σ_s as the Horvitz-Thompson estimator for one-sigma confidence bounds in such a poll plan. The computation of σ_s with the Horvitz-Thompson estimator assumes independence of the observations, which is presumably fallacious for our use case, but undoubtedly useful to account for sampling-induced uncertainty.

Assuming independence of the uncertainty sources, we finally apply the law of propagation of uncertainty to evaluate the total uncertainty $\sigma = \sqrt{\sigma_w + \sigma_d + \sigma_b + \sigma_m + \sigma_s}$. This yields one-sigma sensitivity intervals, centered on the mean ensemble estimates, at [7.9 - 9.1] Mt CH_4 yr^{-1} and [8.0 - 9.2] Mt CH_4 yr^{-1} .

Alternatively, sensitivity intervals can be produced by simply computing the mean yearly estimates with respect to all the parameter sets previously described. We added to this ensemble the estimates produced by the ridge regression setting (see next section). This yields an ensemble of 12 estimates, whose distribution is represented by a box plot at Figure S11. From the lower and upper fences (corresponding to the 10%-90% percentile), we derive an interval at [7.1-10.5] Mt CH_4 yr^{-1}. It is noteworthy that both intervals do not account for the same quantities (resp. one sigma and 80% sensitivity bounds), hence their amplitude discrepancy. In addition, the latter does not properly account for the sensor error and the sampling uncertainty, but is better at catching the temporal dependence of the various scenario.

The condition numbers and the degrees of freedom for signal (DOFS; defined as $trace(I - \tilde{S}_\lambda S_p^{-1})$ where I is the identity matrix) of the quadratic programs solved in the inversions are qualitative indicators for the sensitivity of the results produced. These are discussed in the "Validation" section.

Inversion with no prior knowledge on methane emission source rates

Prior knowledge on methane emission sources is required to apply the full inversion methodology presented in this paper. This is a limiting factor as accurate and up-to-date inventory data might be unavailable. We present in this section a more generic framework, where the Bayesian prior is replaced by a $L2$-penalization. This is a simplification of the quadratic program presented in this manuscript, by setting $S_O = I_n$, $S_p = I_n$ and $x_p = 0$. The minimization problem becomes a ridge regression:

$$\begin{array}{ll} min_x & J(x) = \| y - Kx \|_2^2 + \lambda \| x \|_2^2 \\ s.t. & x \geq 0 \end{array}$$

where we only consider as potential emitters the pixels where relevant activity is detected. The second term of the objective function loses its prior information but keeps its regularizing role. This framework is particularly useful for areas where intensive methane activity evolves quickly (e.g. shale oil and gas basins in the USA), and where precise inventory might not be available whereas satellite sensors can derive precise ground activity data (e.g. flaring detected from the VIIRS sensor[45]).

Results and metrics from this framework are presented at Figure S6. The estimated yearly emissions are slightly smaller in the ridge regression setting than in the Bayesian framework (resp. 8.2 Mt CH_4 yr^{-1} and 8.8 Mt CH_4 yr^{-1} in 2019 and 2020 in the ridge regression setting against 8.6 Mt CH_4 yr^{-1} and 9.0 Mt CH_4 yr^{-1} in 2019 and 2020 in the Bayesian framework). The image-per-image correlation of the reconstructed methane images with observed TROPOMI data is slightly higher in the ridge setting at 0.74, as is the correlation of averaged images (0.86 against 0.83). By construction, the DOFS values are significantly higher in the pure ridge regression model (range [35-140], mean value at 99).

Figure S7 shows that differences between spatial emission rates estimated by both settings have absolute values mostly below 200 g CH_4 m^{-2} yr^{-1}. Outputs of the ridge regression setting have a higher spatial volatility (shown by the alternance of negative and positive values on neighboring grid cells on Figure S7, as well as the differences between panels (e) and (f) of Figure S6) due to the absence of prior on emission rates.

Validation

To assess the validity and robustness of the results, we compute a series of metrics and indicators. This includes the distribution of correlations between observed TROPOMI images and prior and posterior reconstructed images (Figure 2); the correlation between the mean observed

image and the mean reconstructed images (Figure 2D); and the percentage of reconstructed methane with respect to observed images (Figure 2E). On average, the mean image-per-image correlation increases from 0.31 (prior reconstruction) to 0.71 (posterior reconstruction) after the optimization process. The same metrics on averaged images rises from 0.42 to 0.83, hence validating the ability of the model to explain local methane enhancements by emissions originating in coal mining areas. The mean posterior percentage of methane reconstructed is 76%, thus indicating that a minor part of the observed methane enhancements is not explained by coal mining emissions.

The condition number criterion is discussed and supported in Figures S9 and S10. In particular, we show that this criterion leads to λ parameters mostly comprised in $\{10^{-2},10^{-1},1\}$, hence efficiently improving the conditioning of the quadratic programs without over-penalizing the objective function (which would artificially lower the emissions estimates). Likewise, the distribution of the DOFS of the system has a lower bound at 20 with a mean value at 75. It shows that the quadratic programs are well-constrained, namely that output of the optimization problem is largely influenced by TROPOMI images and not primarily determined by the prior term (see Figure S10).

Figures 2 and 3 reveal a high stability in the estimates, both monthly and hourly, aggregated and on a gridded basis (standard deviation of the monthly estimates is 0.11Mt). This is expected as ventilation air methane systems are set to continuously ventilate coal mines, and it argues for the robustness of the inversion estimates.

We show that the results have a very low sensitivity to the construction of the minimization problem. A pure ridge regression setting ($S_O = I_n$, $S_p = I_n$ and $x_p = 0$) produces very similar methane emission estimates and validation metrics (see Figures S6 and S7).

In the inversion, we only consider coal mines to be responsible for the methane emissions we measure. The rationale is that 1) emissions from coal represents 92% of the methane emissions in Shanxi according to the EDGAR v6.0 database; 2) at the grid pixel level, methane emissions from non-coal sources are two orders of magnitude smaller than methane emissions from coal sources (see Figure S12). Emissions from other sources have a very high spatial regularity (see Figure S12), hence they mainly contribute to the background methane value which is removed in the methane enhancement images used in our inversion.